Vita

Education

- Ph.D., Materials Science and Engineering, *Pennsylvania State University, PA, USA* (2017)
- M.S., Physics, *National Taiwan University, Taiwan* (2011)
- B.S., Physics, *National Cheng Kung University, Taiwan* (2009)

Research Experiences

Pennsylvania State University, University Park, PA (January 2013–August 2017)
Graduate Research Assistant

- Performed epitaxial growth of two-dimensional (2D) materials by chemical vapor deposition
- Studied properties of 2D and relevant nanomaterials via optical and electrical characterizations
- Fabricated and measured transistors and diodes of 2D materials

National Taiwan University, Taiwan (June 2009–June 2011)
Graduate Research Assistant

- Synthesized graphene and graphene oxide and studied their electrical properties
- Performed device fabrication
- Investigated the magneto-transport on the 2D electron system in GaAs/AlGaAs

© Springer Nature Switzerland AG 2018

Y. -C. Lin, *Properties of Synthetic Two-Dimensional Materials and Heterostructures*, Springer Theses,
https://doi.org/10.1007/978-3-030-00332-6

National Cheng Kung University, Taiwan (June 2007–June 2009)
Undergraduate Research Assistant

- Investigated the impact of the geometry of defective AFM tips on imaging $BiFeO_3$

Teaching and Mentorship

Pennsylvania State University, University Park, PA (Fall 2015 and 2016)
"Metallurgical Laboratory" with the instructor, Amy C. Robinson

- Led two sessions weekly for a class of 20 undergraduates majored in Materials Sciences
- Prepared lab materials and taught lectures to students prior to the lab

National Taiwan University, Taiwan (Fall 2009–Spring 2011)
"Quantum Mechanics" at graduate level, with Professor Jeng-Wei Chen
"Electromagnetism" at undergraduate level, with Professor Jeng-Wei Chen

- Engaged students in the office hours; graded exams and homework

Student Researcher Mentees

- Jennifer G. DiStefano (Penn State undergraduate, January 2013–May 2016)
- Kursti S. DeLello (Univ. of Central Florida undergraduate, REU, May 2016–August 2016)
- Jing-Kai Huang (National Chiao-Tung Univ. master degree, May 2010–December 2011)

Award

- Graduate Student Award Silver Medalist, Materials Research Society, *USA* (2016)

Selected Publications

1. Y.-C. Lin, R. Addou, Q. Wang, C. Smyth, S. M. Eichfeld, Ganesh R. Bhimanapati, M. J. Kim, R. M. Wallace, J. A. Robinson, "Novel defect-mediated transport in van der Waals heterostructures" (Submitted 2019)
2. Y.-C. Lin,† B. Jariwala,† B. M. Bersch, K. Xu, Y. Nie, B. Wang, S. M. Eichfeld, X. Zhang, T. Choudhury, Y. Pan, R. Addou, C. M. Smyth, J. Li, K. Zhang, A. Haque, S. Fölsch, R. M. Feentra, R. M. Wallace, K. Cho, S. K. Fullerton,

J. M. Redwing, J. A. Robinson, "Large-area, Electronic-grade Two-dimensional Semiconductors", ***ACS Nano*** (2018) († Equal contribution)

3. B. M. Bersch,† S. M. Eichfeld,†Y.-C. Lin,† K. Zhang, G. R. Bhimanapati, A. F. Piasecki, M. Labella III, J. A. Robinson, "Selective area growth and controlled substrate coupling of transition metal dichalcogenides" ***2D Materials*** (2017), 4, 025083 († Equal contribution)
4. Y.-C. Lin, K. DeLello, H.-T. Zhang, K. Zhang, J. A. Robinson, "Photoluminescence of monolayer transition metal dichalcogenides integrated with VO_2" ***Journal of Physics: Condensed Matter*** (2016), 28, 50
5. Y.-C. Lin, J. Li, S. C. de la Barrera, S. M. Eichfeld, Y. Nie, R. Addou, P. C. Mende, R. M. Wallace, K. Cho, R. M. Feenstra, J. A. Robinson, "Tuning electronic transport in epitaxial graphene-based van der Waals heterostructures" ***Nanoscale*** (2016), 8, 8947
6. Y.-C. Lin, R. K. Ghosh, R. Addou, N. Lu, S. M. Eichfeld, H. Zhu, M.-Y. Li, X. Peng, M. J. Kim, L.-J. Li, R. M. Wallace, S. Datta, J. A. Robinson, "Atomically thin resonant tunneling diodes built from synthetic van der Waals heterostructures" ***Nature Communications*** (2015), 6, 7311
7. Y.-C. Lin, C.-Y. S. Chang, R. K. Ghosh, J. Li, H. Zhu, R. Addou, B. Diaconescu, T. Ohta, X. Peng, M. J. Kim, J. T. Robinson, R. M. Wallace, T. S. Mayer, S. Datta, L.-J. Li, J. A. Robinson, "Atomically thin heterostructures based on single-layer tungsten diselenide and graphene" ***Nano Letters*** (2014), 14, 6936–6941
8. Y.-C. Lin, N. Lu, N. Perea-Lopez, J. Li, Z. Lin, C. H. Lee, C. Sun, L. Calderin, P. N. Browning, M. S. Bresnehan, M. J. Kim, T. S. Mayer, M. Terrones, J. A. Robinson, "Direct synthesis of van der Waals Solids" ***ACS Nano*** (2014), 8, 3715–3723

Appendices

Appendix A

Parameters of MOCVD Process for Epitaxial WSe_2

A controlled layer-by-layer growth of WSe_2, ranging from monolayer to three layers, was achieved by following the growth profile illustrated in Fig. A.1. Growths were done at 700 Torr using H_2 as a carrier gas, where $W(CO)_6$ and H_2Se precursors are introduced separately into the cold wall vertical reactor chamber and their respective flow rates controlled via mass flow controllers (MFCs). The optimized condition for the growth was modified from our previously reported work [1]. In order to achieve uniform deposition with complete coalescence over the entire

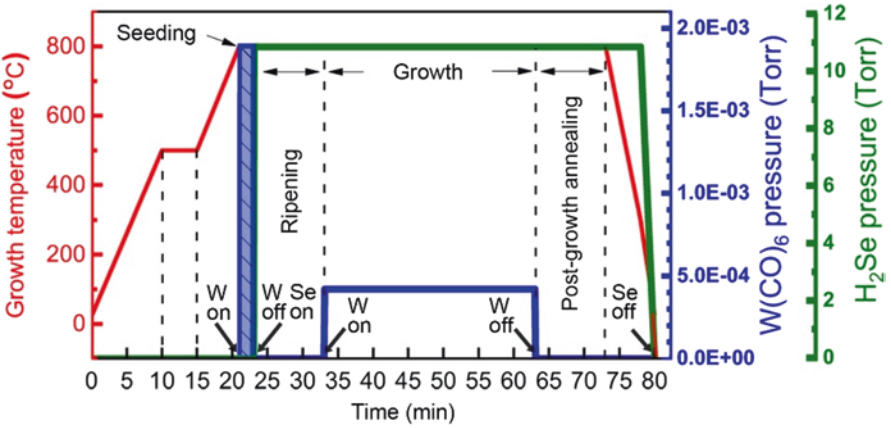

Fig. A.1 Optimized growth profile for MOCVD process of monolayer epitaxial WSe_2 grown on sapphire [2]

© Springer Nature Switzerland AG 2018

Y. -C. Lin, *Properties of Synthetic Two-Dimensional Materials and Heterostructures*, Springer Theses,
https://doi.org/10.1007/978-3-030-00332-6

substrate area, we introduce a step that combines seeding and annealing at 800 °C where the substrate is exposed to partial pressures of ~2 × 10^{-3} Torr W-precursor and 11 Torr H_2Se for 30 s to 2 min, named "pregrowth seeding step." Subsequently the WSe_2 is annealed in H_2Se to allow the nucleated domain to grow further under Se-rich environment. Also, such pre-annealing step at higher temperature acts as a surface treatment on c-sapphire surface and promotes Se passivation of the sapphire, which further acts as bridge for epitaxy at 2D/3D interface (detail can be found in main text). The number of layers was controlled by varying the seeding time, 30 s (1L) to 2 min (3L), while keeping growth time 30 min unchanged. All growths were done at 800 °C and 730 Torr total pressure with constant W:Se flux by adjusting the $W(CO)_6/H_2Se$ partial pressure individually for the following layer number: 4.32 × 10^{-4} Torr/10.8 Torr (1L), 6.24 × 10^{-4} Torr/15.6 Torr (2L), and 7.68 × 10^{-4} Torr /19.2 Torr (3L). Growth profile in Fig. A.1 is representative of deposition conditions for monolayer WSe_2 film.

Theoretical Modeling

The density functional theory (DFT) calculations were performed with the Vienna ab initio simulation package (VASP) [3]. The valence electronic states are expanded in a set of periodic plain waves, and the ion-electron interaction is implemented through the projector-augmented wave (PAW) approach [4]. The Perdew-Burke-Ernzerhof (PBE) GGA exchange-correlation functional is applied in the simulation [5]. The wave functions are expanded in plane waves with a kinetic energy cutoff of 400 eV. The convergence criteria for the electronic and ionic relaxation are 1.0 × 10^{-5} eV and 1.0 × 10^{-4} eV, respectively. Integration over the first Brillouin zone is performed with a Γ-centered 3 × 3 × 1 k-point mesh. A supercell consisting of 2 × 2 α-Al_2O_3 unit cells and 3 × 3 1L WSe_2 unit cells is built with a 4% strain on WSe_2. A vacuum layer of 20 Å is added to the c-direction. To avoid long-range interactions between supercells, a supercell consists of the surface and interface under study on both sides along the *c*-direction. The proposed WSe_2-sapphire interfaces based on the EDX data (Fig. A.2) are shown in Fig. A.3. Except for the Al-terminated sapphire/WSe_2 interface, gap states exist within the bandgap of WSe_2 after contact. Comparing the density of states

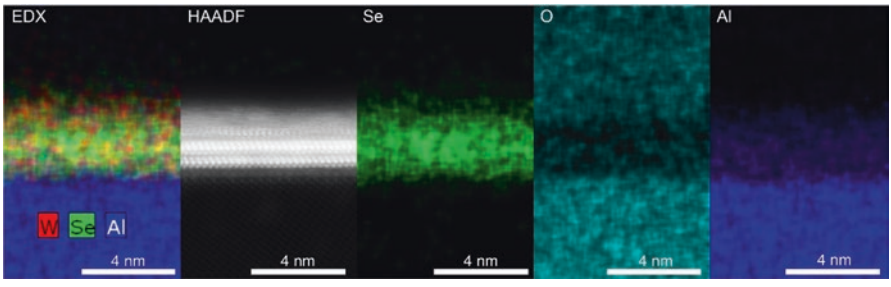

Fig. A.2 EDX and HAADF image captured from the same section during STEM measurement at 200 kV identify the distribution of W, Se, Al, and O [2]

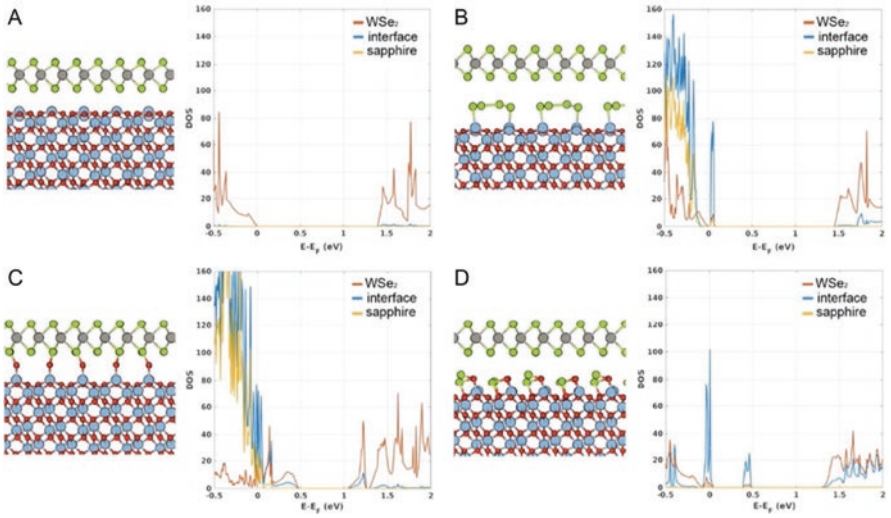

Fig. A.3 DFT modeling for 2D/3D interface. The proposed interface structures and their corresponding density of state (DOS) under different terminations: (**a**) Al-terminated (**b**) Al-Se-terminated (**c**) O-terminated (**d**) Al-O-Se-terminated. The 0 eV is the valence band edge for an intrinsic semiconductor [2]

of the gap states, the four interfaces are ordered as Al-O > Al-Se > Al-O-Se > Al. The calculations indicate that the interaction (bonding) energy between WSe_2 and the Se-terminated sapphire surfaces (4.23 eV for Al-Se connection in Fig. A.3b and 2.6 eV for Al-O-Se connection in the d) lies between that of WSe_2/Al-terminated (0.04 eV) and WSe_2/Al-O-terminated surfaces (5.4 eV). This relatively high interface bonding energy between WSe_2 and Al-Se connection also manifests itself mechanically, as we find that fully coalesced epitaxial WSe_2 layers are more difficult to mechanically transfer from the substrate than non-epitaxial WSe_2.

Device Fabrication

Field-effect transistors were fabricated via standard photolithography to define WSe_2 channel dimensions, source/drain (S/D) contact electrodes, and side-gate electrodes (Fig. 3.14). The 4.1 × 2.5 mm die layout employed in this work consists of an array of FETs with channel width 24 μm and channel length ranging from 10 μm to 0.75 μm. With these die dimensions in mind, a 3 row × 2 column die layout is used to cover a majority of the 10 × 10 mm sample surface. In our work, the gate electrode is not directly deposited on top of the electrolyte-WSe_2 FETs, and instead, we utilize a side-gate geometry that establishes a lateral electric field in the PEO:$CsClO_4$ (PEO: poly(ethylene-oxide)) and drives the ions into place on the WSe_2 channel surface. All photolithography was carried out in a GCA 8500 i-line stepper. WSe_2 channels were isolated and etched via reactive ion etching in a Plasma Therm PT-720 plasma etch tool using an SF_6/O_2/Ar gas chemistry at 10 mTorr and

100 W for 30 s. Both 25 nm Ni and 10/10 nm Pd/Au source/drain metallizations are carried out under moderate vacuum (~10^{-6} Torr) at 1.0 Å/s dep rate. Directly prior to loading samples into evaporator for metal deposition and eventual lift-off, samples are subjected to a brief oxygen plasma treatment to remove photoresist residue that remains on the WSe_2 surface following photoresist development. This gentle plasma treatment/surface prep is carried out in an M4L etch tool at 50 W and 500 mTorr for 45 s. Following this initial metal deposition, a second metallization consisting of ~10 nm/150 nm Ti/Au is carried out to define the side gate and to thicken source/drain pads for probing.

Appendix B

Computational Methods for the Intrinsic Dipoles Between WSe_2 and Graphene

The density functional theory (DFT) calculation is performed by Vienna ab initio simulation package (VASP) [3] with the projector-augmented wave (PAW) method [4]. The local density approximation (LDA) [6] is used to describe the exchange-correlation functional with the partial core correction included. Spin polarization and spin-orbit coupling are applied. The stable phase of the monolayer WSe_2 is trigonal prism structure [7]. The optimized planar lattice constant of WSe_2 is 3.25 Å, and the optimized planar lattice constant for monolayer graphene is 2.45 Å. In order to fit the lattice constant, a supercell with 3 × 3 WSe_2 unit cells and 4 × 4 graphene unit cell is used, and a compressive strain of 0.4% is applied to graphene, as the electronic behaviors of TMDC are very much susceptible to lattice strain. The supercell is shown in Fig. B.1a. The wave functions are expanded in plane waves with a kinetic energy cutoff of 500 eV, and the convergence criteria for the electronic relaxation are 10^{-5} eV. Integration over the Brillouin zone is performed with a gamma-centered 6 × 6 × 1 Monkhorst-Pack k-point mesh for ionic and electronic optimization. A vacuum region of about 15 Å normal to the surface is added to minimize the interaction between adjacent slabs (Fig. B.1a). Dipole correction on the stacking direction is used in systems to reveal the dipole within the two layers caused by the Fermi-level alignment. The local density approximation (LDA) is found to be suitable for studying the metal-TMDC contact [8]. The generalized gradient approximation (GGA) [5] with the DFT-D2 method for van der Waals (vdW) corrections [9] is also used to cross-check the structural accuracy. We find that GGA results with vdW corrections are in overall agreement with LDA results. Both the LDA method and the GGA + vdW method result in a similar structure with a distance of ~3.5 Å between graphene and TMDC, indicating a secondary bond interaction. The energy difference between the vacuum regions on the both sides of the contact system is the dipole induced by the contact. The vacuum energy level above WSe_2 is 0.17 eV higher than that above graphene, indicating a dipole from graphene toward the WSe_2 (Fig. B.1b).

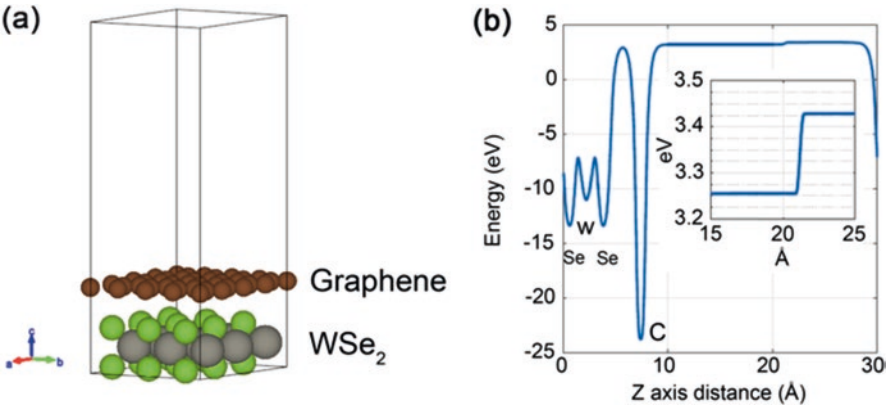

Fig. B.1 (**a**) Plane averaged local electric potential energy of electrons along the stacking direction. (**b**) After dipole correction, a difference on vacuum energy above both sides of 0.17 eV is observed (zoomed inset) [10]

Computation of WSe_2 Doping Density and Charge Densities and Dependence on Parameters

For the computation of charge transfer and band alignment, we take the doping densities of EG_{PH} and EG_{FH} from our experimental values, as discussed in the main text. Parameters in the computation are the electron affinities for monolayer and bilayer graphene, with nominal values of 4.57 eV and 4.71 eV, respectively, as known from prior experiments [11]. We take the sum of the electron affinity plus bandgap of the WSe_2, $\chi_{WSe_2} + E_g$, to be an unknown in the computation, since a value for this sum is not accurately known from prior work (only the sum is considered here since the electron occupation in the conduction band of the WSe_2 is negligible). A second unknown is the unintentional doping density of WSe_2. Then, using the two measured work function differences for WSe_2 on both EG_{PH} and EG_{FH} compared to the bare EG_{PH} and EG_{FH}, we can determine values for the two unknown parameters. The carrier densities for the WSe_2 on both EG_{PH} and EG_{FH} after charge transfer are then a byproduct of the computation. In all cases, the carrier densities of WSe_2 in WSe_2-EG_{PH} are very much greater than those of WSe_2 in WSe_2-EG_{FH}, consistent with the observed differences in the CAFM *I–V* results.

We note that the doping density values in Table B.1 are all the same, reflecting a tight constraint on this value. This constraint arises from charge transfer between the WSe_2 and the EG_{PH}. As pictured in Fig. B.2a, b, since the Fermi energies of the EG_{PH} and WSe_2 are relatively far apart prior to charge transfer, and hence the Fermi energy of the WSe_2 ends up well within its bandgap after the transfer, then the p-type doping density in the WSe_2 is directly determined by the doping density of the EG together with the difference between the electron affinity of the EG_{PH} and the $\chi_{WSe_2} + E_g$ value of the WSe_2. The resulting carrier densities for the WSe_2 on EG_{PH} are negligible, again since the resulting WSe_2 Fermi energy is well within the gap. On the other hand, for the WSe_2 on EG_{FH}, their Fermi energies are relatively close prior to charge transfer, as pictured in Fig. B.2c, d. The resulting Fermi energy for

Table B.1 Computed dependence of electron affinity plus bandgap of WSe_2 ($X_{WSe_2} + E_g$), unintentional doping of WSe_2 (N_A), carrier density of WSe_2 after charge transfer between WSe_2 and EG_{PH} ($N_{C,WSe_2-EG_{PH}}$), and carrier density of WSe_2 after charge transfer between WSe_2 and EG_{FH} ($N_{C,WSe_2-EG_{FH}}$) on electron affinities of EG_{PH} ($X_{EG_{PH}}$) and EG_{FH} ($X_{EG_{FH}}$), respectively

$X_{EG_{PH}}$ (eV)	$X_{EG_{FH}}$ (eV)	$X_{WSe_2} + E_g$ (eV)	N_A (cm^{-2})	$N_{C,WSe_2-EG_{PH}}$ (cm^{-2})	$N_{C,WSe_2-EG_{FH}}$ (cm^{-2})
4.57	4.71	5.09	1.3×10^{12}	4.1×10^{5}	2.9×10^{12}
4.47	4.71	5.09	1.3×10^{12}	0.9×10^{4}	2.9×10^{12}
4.67	4.71	5.09	1.3×10^{12}	2.0×10^{7}	2.9×10^{12}
4.57	4.61	4.99	1.3×10^{12}	2.0×10^{7}	2.9×10^{12}
4.57	4.81	5.19	1.3×10^{12}	0.9×10^{4}	2.9×10^{12}

An error range of ±0.1 eV for the input parameters is considered [12]

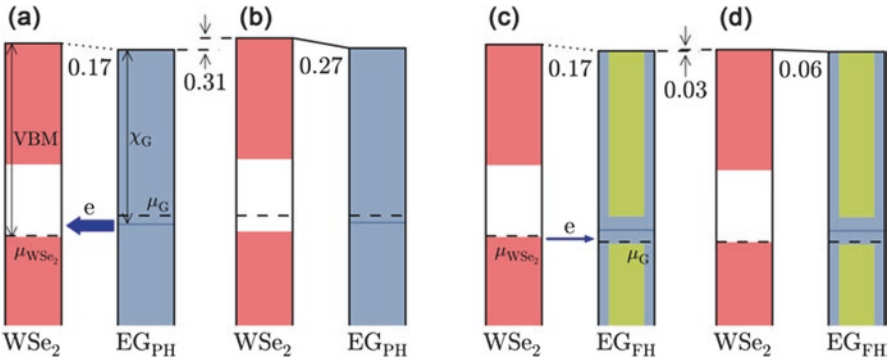

Fig. B.2 Band alignment of WSe_2 and EG_{PH} (**a**) before charge transfer (including computed intrinsic dipole 0.17 eV) and (**b**) after charge transfer. Band alignment of WSe_2 and EG_{FH} (**c**) before charge transfer (including the intrinsic dipole) and (**d**) after charge transfer. Monolayer and bilayer graphene models are employed for EG_{PH} and EG_{FH}, respectively, based on LEEM observations. Green shades in (**c**) and (**d**) represent conduction/valence subbands of bilayer graphene. The numerical values show various vacuum level differences, in units of eV [12]

the WSe_2 on EG_{FH} ends up near or within the valence band even after the charge transfer, with concomitant large carrier density, and the value of the WSe_2 doping density is not so tightly constrained in this part of the problem.

We have also considered the effect on the computed carrier densities of variation in the EG_{PH} and EG_{FH} doping density values, as well as variation of the measured work function differences within their experimental error ranges. Doping densities of $(4 \pm 1) \times 10^{12}$ cm^{-2} for EG_{PH} and $(1.5 \pm 0.2) \times 10^{13}$ cm^{-2} for EG_{FH} are typical measured in our samples. Considering the variations of these doping densities, the carrier density of WSe_2 on EG_{FH} after charge transfer is computed to range from 2.5 to 3.0×10^{12} cm^{-2}, while the carrier density of WSe_2 on EG_{PH} after transfer is always less than 10^{7} cm^{-2}, i.e., its Fermi is well within the bandgap. For the measured error ranges (±0.03 eV) on the work function differences, performing computations at the bounds of these values produces carrier densities in the WSe_2 on EG_{FH} compared to WSe_2 on EG_{PH} that continue to differ by more than a factor of 10^{4}, for all cases.

Appendix C

Theoretical Validation for NDR Transport in the Trilayer Structures

We perform non-equilibrium ballistic quantum transport calculations by combining density functional theory (DFT) with the non-equilibrium Green's function (NEGF) formalism that provide theoretical *I–V* curves to confirm the NDR transport mechanism in the heterostructure by comparing it against the simulated transport in the homo-structure (Fig. C.1). In the experimental setup, the voltage, V_{ds}, is applied between the *Pt-Ir* tip of the conducting AFM and the electrically grounded graphene electrode. The area of the *Pt-Ir* tip is approximately to 1000 nm^2, which in the simulation is modeled as a bulk electrode in the theoretical structure (Fig. C.1a). The calculation produces the bias and the transverse momentum-dependent transmission probability of the carriers tunneling through the heterostructure and is used to simulate the *I–V* characteristics using Landauer transport formulation [13]:

$$I\left(V_{ds}\right) = \frac{2q}{h} \int_{BZ} dk \int dE T\left(E,,k\,,,V_{ds}\right)\left[f\left(\frac{E - E_{f_1}}{k_B T}\right) - f\left(\frac{E - E_{f_2}}{k_B \boldsymbol{T}}\right)\right], \qquad \text{(C.1)}$$

where $E_{f_1} - E_{f_2} = qV_{ds}$ represents the Fermi window, BZ represents the Brillouin zone, and $T(E,k||,V_{ds})$ is the total transmission over the energy channels within the Fermi window calculated self-consistently for each V_{ds}. Within the NEGF + DFT framework for transport, the Hamiltonian of the system is solved by calculating the electronic charge distribution via the self-consistent DFT loop of the full density matrix of the device whose diagonal element describes the charge density.

This procedure produces the bias-dependent transmission function, $T\,(E, V, k||)$. We then extract the *I–V* characteristics in the ballistic transport regime which shows a pronounced NDR in both positive and negative bias regimes of the MoS_2-WSe_2-Gr heterostructure device (Fig. C.1b). Within the Fermi window of 0–0.4 eV, we can see that the carrier transmission is effectively negligible due to the absence of any transmission channel. Above 0.4 eV, the transmission becomes finite, and the current starts increasing with the applied bias, where the primary transmission resonance peaks (peak P1, P2, and P3 in Fig. C.1c) appear at approximately 1.0 V and then get suppressed with further increase in applied bias. It is this peak and valley in the transmission spectra arising from resonant tunneling phenomenon that leads to the observed NDR. When the bias is further increased, conventional tunneling occurs due to the high density of states (DOS) at higher energy levels, and the current increases exponentially thereafter. The transmission Eigen states at the energetic location of the three strong peaks for a bias of +1.0 V provide clue to the microscopic origin of the NDR in the MoS_2-WSe_2-Gr heterostructure. Inspection of the localized molecular orbitals of the Eigen states (Fig. C.1d) reveals that all three resonance peaks originate from a combination of the Pt electrode (*s*-orbital), WSe_2 (*p*-orbital of Se, W and *d*-orbital of W), and graphene layers (*p*-orbital).

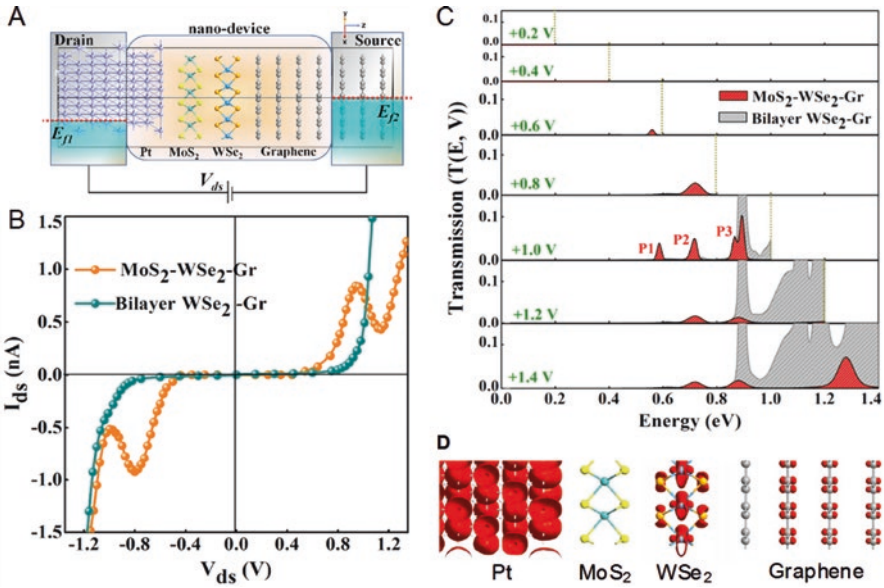

Fig. C.1 (**a**) Schematic of the vertical nano-device setup of both of MoS_2-WSe_2-Gr and bilayer WSe_2-Gr system used for quantum transport calculation. E_{f_1} and E_{f_2} indicate the corresponding Fermi levels of the left and right electrodes, respectively, for an applied positive bias V_{ds}. (**b**) Theoretical *I–V* curves of the vertical tunnel junctions for both the hetero- and homo-junction are simulated by the DFT and NEGF transport formalism that give resonant tunneling at specific energies and bias voltage, as shown in (**c**). The dotted line indicates the Fermi window for that applied bias voltage across the terminals. (**d**) Transmission Eigen states that contribute to the transmission in the peak P3 of the transmission at V_{ds} = +1.0 V in the MoS_2-WSe_2-Gr heterostructure [14]

In the case of MoS_2-WSe_2-Gr heterostructure, the MoS_2 in direct contact with the Pt electrode and the first graphene layer closest to the WSe_2 do not contribute to the strong transmission peaks but serve as tunnel barriers. Furthermore, the interatomic electronic interaction between the 2D layers makes MoS_2 n-type and WSe_2 p-type, which make the WSe_2 valence band states as the host for the confinement of the resonant states when the system is subjected to a bias. Along with the conservation of transverse momenta and the alignment of energy levels in the constituent layers of the system, the theoretical *I–V* traces are in good agreement with the measured results. On the other hand, bilayer WSe_2 does not offer any band offset in the energy band diagram, and its bandgap acts as a regular electronic barrier in the carrier tunneling. The calculated transmission in bilayer WSe_2-Gr clearly reflects this nature and shows no NDR in its *I–V* characteristics. This study hence provides strong theoretical insights that show resonant tunneling is the dominant transport mechanism in a heterostructure with significant amounts of band offset.

References

1. Eichfeld, S.M., et al.: Highly scalable, atomically thin WSe_2 grown via metal-organic chemical vapor deposition. ACS Nano. **9**, 2080–2087 (2015)
2. Lin, Y.C., et al.: Realizing large-scale, electronic-grade two-dimensional semiconductors. ACS Nano. **12**, 965–975 (2018)
3. Kresse, G., Furthmüller, J.: Efficient iterative schemes for ab initio total-energy calculations using a plane-wave basis set. Phys. Rev. B. **54**, 11169–11186 (1996)
4. Kresse, G., Joubert, D.: From ultrasoft pseudopotentials to the projector augmented-wave method. Phys. Rev. B. **59**, 1758–1775 (1999)
5. Perdew, J.P., Burke, K., Ernzerhof, M.: Generalized gradient approximation made simple. Phys. Rev. Lett. **77**, 3865 (1996)
6. Ceperley, D.M., Alder, B.J.: Ground state of the electron gas by a stochastic method. Phys. Rev. Lett. **45**, 566–569 (1980)
7. Gong, C., et al.: Band alignment of two-dimensional transition metal dichalcogenides: application in tunnel field effect transistors. Appl. Phys. Lett. **103**, 053513 (2013)
8. Gong, C., Colombo, L., Wallace, R.M., Cho, K.: The unusual mechanism of partial Fermi level pinning at metal-MoS_2 interfaces. Nano Lett. **14**, 1714–1720 (2014)
9. Makov, G., Payne, M.: Periodic boundary conditions in ab initio calculations. Phys. Rev. B. **51**, 4014–4022 (1995)
10. Lin, Y.-C., et al.: Tuning electronic transport in epitaxial graphene-based van der Waals heterostructures. Nanoscale. **8**, 8947–8954 (2016)
11. Yu, Y.-J., et al.: Tuning the graphene work function by electric field effect. Nano Lett. **9**, 3430–3434 (2009)
12. Lin, Y.-C., et al.: Wafer-scale MoS_2 thin layers prepared by MoO_3 sulfurization. Nanoscale. **4**, 6637 (2012)
13. Datta, S.: Quantum transport-atom to transistor. Cambridge University Press, Cambridge (2005)
14. Ghosh, R.K., Lin, Y.-C., Robinson, J.A., Datta, S.: Heterojunction resonant tunneling diode at the atomic limit. International Conference on Simulation of Semiconductor Processes and Devices (SISPAD), 266–269. IEEE (2015)

© Springer Nature Switzerland AG 2018

Y. -C. Lin, *Properties of Synthetic Two-Dimensional Materials and Heterostructures*, Springer Theses,
https://doi.org/10.1007/978-3-030-00332-6